

# Spectral Properties of Effective Dynamics from Conditional Expectations

Feliks Nüske · Péter Koltai · Lorenzo Boninsegna ·  
Cecilia Clementi

the date of receipt and acceptance should be inserted later

**Abstract** The reduction of high-dimensional systems to effective models on a smaller set of variables is an essential task in many areas of science. For stochastic dynamics governed by diffusion processes, a general procedure to find effective equations has recently been suggested in *Legoll and Lelièvre, Nonlinearity, 2010*. In this study, we investigate the approximation of slowly varying modes by the effective dynamics, which are associated to low-lying eigenvalues of the associated generator. Slowly varying variables are of particular interest in a variety of research fields, including molecular simulation. We prove a new relative error bound for these eigenvalues in the reversible setting. Moreover, we discuss the applicability of these results to Langevin dynamics, which is a highly popular model in molecular dynamics. We illustrate our findings on several benchmark systems. These examples provide further insights about parameter estimation for the effective dynamics.

## 1 Introduction

The description of high-dimensional systems by a reduced set of variables, usually referred to as *coarse graining*, is of tremendous importance across many different fields of research. Examples range from finance to climate modeling to molecular biology. Two of the central reasons for the importance of coarse graining are that, firstly, analysis or numerical simulation of high-dimensional systems is often challenging or simply infeasible, and secondly, not all detailed features of the full system are needed in order to answer questions of scientific interest. Typical challenges arising along the search for a coarse grained model are 1) which properties of the high-dimensional system are important, and which ones are not, 2) what constitutes a good set of reduced variables (also called *collective variables* or *reaction coordinates* in some contexts), and 3) what is a suitable equation to define the low-dimensional description of the system, often called an *effective dynamics*.

In this paper, we will study the coarse graining problem for systems driven by a diffusion process, and adopt a perspective motivated by molecular dynamics simulations of biological systems. In molecular simulation, equilibrium properties and slow dynamical properties are typically identified as relevant, while all fast oscillatory or vibrational motions are less important to characterize the long-time behavior of the system. We will approach the second and third question raised above from this perspective.

For molecular systems, two types of coarse graining strategies can be broadly distinguished. The first is coarse graining in structural space, where the physical representation of a system is simplified, e.g. by unifying several atoms into so-called beads or pseudo-atoms, see e.g. [9, 31, 40]. The second approach is a coarse graining in configurational space. Here, the full system is projected to a smaller set of variables by a transformation of its state space. Important contributions along these lines are the Mori–Zwanzig formalism [26, 48, 7, 8, 18] as well as the framework of averaging and homogenization for systems with explicit multiscale structure [33]. For further important contributions to this line of research in the field of molecular simulation please see [37, 39, 29] and the references therein. We proceed along the latter direction and concentrate on the effective dynamics using

---

Feliks Nüske · Lorenzo Boninsegna · Cecilia Clementi  
Center for Theoretical Biological Physics, and Department of Chemistry, Rice University, 6100 Main St, Houston, TX, 77005, United States,  
E-mail: feliks.nueske@rice.edu, cecilia@rice.edu

Péter Koltai  
Department of Mathematics and Computer Science, Freie Universität Berlin, Arnimallee 6, 14195 Berlin, Germany

conditional expectations introduced in [22] and discussed in detail in Refs. [47, 23]. In particular, we focus on the preservation of slow dynamical components by the effective dynamics.

The contribution of this paper is as follows: first, we discuss the error between dominant eigenvalues of the full and the effective dynamics for reversible diffusions. We provide a new bound for the relative approximation error of the dominant eigenvalues in terms of the  $H_\mu^1$ -approximation error for the corresponding eigenfunctions. The relative error is a more practical error measure for small eigenvalues than the absolute error considered in [47]. Also, the new bound is less restrictive than the one obtained therein.

Second, we discuss the applicability of these results to Langevin dynamics if their overdamped limit is exploited, which requires the use of a large offset when estimating the parameters of the effective dynamics by Kramers–Moyal type estimators.

Third, we present numerical examples showing that essential long-term dynamical properties appear to be preserved well by effective dynamics estimated using a large offset. This observation makes the second point particularly useful. Although a theoretical proof of these findings is still lacking, as a potential first step, we provide expressions for the parameters of the effective dynamics at large offset within metastable sets.

The rest of this paper is organized as follows: in section 2, we recap what is needed of the theory of diffusion processes, their generators and transfer operators. Section 3 contains a description of the effective dynamics, our approximation result, the discussion of Langevin dynamics and the expressions for large offsets. Numerical results for two toy problems and two benchmark datasets of molecular dynamics simulation are provided in section 4. Conclusions and outlook follow in section 5.

## 2 Stochastic Dynamics

### 2.1 Setting

In this paper, we consider a continuous-time and -space Markov process  $X_t$  attaining values in  $\mathbb{R}^d$ . The process is governed by the stochastic differential equation

$$dX_t = b(X_t)dt + \sqrt{2\beta^{-1}}\sigma(X_t)dB_t. \quad (1)$$

Here,  $B_t$  denotes  $d$ -dimensional Brownian motion, the function  $b : \mathbb{R}^d \mapsto \mathbb{R}^d$  is called the drift,  $\beta$  is the inverse temperature, and  $\sigma : \mathbb{R}^d \rightarrow \mathbb{R}^{d \times d}$  is called the diffusion. We use the notation

$$a(x) = \sigma(x)\sigma(x)^T \quad (2)$$

for the covariance matrix of the diffusion. A standard example for dynamics of type Eq. (1) are Langevin dynamics

$$dq_t = p_t dt, \quad (3)$$

$$dp_t = -\nabla V(q_t)dt - \gamma p_t dt + \sqrt{2\gamma\beta^{-1}}dB_t, \quad (4)$$

of a system with  $N$  position variables  $q_t \in \mathbb{R}^N$  and momentum variables  $p_t \in \mathbb{R}^N$ , such that  $d = 2N$ . The constant  $\gamma$  in Eq. (4) represents friction, while the function  $V : \mathbb{R}^N \mapsto \mathbb{R}$  is the potential energy on position space. A second and related example is the overdamped Langevin process

$$dq_t = -\frac{1}{\gamma}\nabla V(q_t)dt + \sqrt{2\beta^{-1}\gamma^{-1}}dB_t, \quad (5)$$

which is defined on position space only, i.e.,  $d = N$ .

We assume that drift and diffusion are smooth functions and that  $a$  is bounded and uniformly elliptic, i.e.,

$$\eta_1 \|v\|^2 \geq v^T a(x)v \geq \eta_2 \|v\|^2, \quad (6)$$

for all vectors  $v \in \mathbb{R}^d$ , and  $\eta_1, \eta_2 > 0$  are independent of  $x$ . It follows that  $X_t$  is ergodic with respect to a unique invariant measure  $\mu$ . Note that the Langevin process Eqs. (3-4) does not satisfy Eq. (6), but ergodicity

can still be shown using different techniques [34, 24].<sup>1</sup> We assume that the invariant measure possesses a density function with respect to Lebesgue measure, likewise denoted by  $\mu$ . We will frequently use the Hilbert space  $L^2_\mu$  of square integrable functions with respect to the measure  $\mu$ , with scalar product

$$\langle f, g \rangle_\mu = \int_{\mathbb{R}^d} f(x)g(x) \, d\mu(x). \quad (7)$$

Also, we use the symbols  $H^k_\mu$  for the Sobolev spaces [16] of functions possessing weak derivatives up to order  $k$  in  $L^2_\mu$ .

The system dynamics are encoded in the semigroup of transfer operators  $\mathcal{T}_\tau$ ,  $\tau \geq 0$ , defined for  $f \in L^2_\mu$  by

$$\mathcal{T}_\tau f(x) = \mathbb{E}^x [f(X_\tau)], \quad (8)$$

where  $\mathbb{E}^x[\cdot]$  denotes expectation given that the dynamics starts deterministically at  $x$ . Transfer operators describe the evolution of expectation values as the dynamics progress over a time window  $\tau$ , typically called the lag time. We denote the infinitesimal generator of this semigroup by  $\mathcal{L}$ , and its domain by  $D(\mathcal{L}) \supset H^2_\mu$ . For twice continuously differentiable functions  $f \in L^2_\mu$ , the generator acts as a differential operator:

$$\mathcal{L}f(x) = b(x) \cdot \nabla f(x) + \frac{1}{\beta} a(x) : \nabla^2 f(x), \quad (9)$$

where  $\nabla^2 f$  is the matrix of second derivatives of the function  $f$  and  $:$  denotes the Frobenius inner product between matrices. A diffusion process is called reversible if the generator is self-adjoint on  $L^2_\mu$ . In this case,  $\mathcal{L}$  satisfies the equality

$$\langle \mathcal{L}f, g \rangle_\mu = -\frac{1}{\beta} \int_{\mathbb{R}^d} a(x) \nabla f(x) \cdot \nabla g(x) \, d\mu(x) \quad (10)$$

for all  $f, g \in D(\mathcal{L})$ . We will assume reversibility from now on.

## 2.2 Spectral Properties

With the assumption (6) the generator  $\mathcal{L}$  has compact resolvents<sup>2</sup> and thus possesses a complete set of eigenfunctions corresponding to isolated eigenvalues. That is, there are functions  $\psi_1, \psi_2, \dots$  and non-negative numbers  $0 = \kappa_1 < \kappa_2 \leq \dots$  such that

$$\mathcal{L}\psi_i = -\kappa_i \psi_i, \quad (11)$$

and every function  $f \in L^2_\mu$  can be represented by the expansion

$$f = \sum_{i=1}^{\infty} \langle f, \psi_i \rangle_\mu \psi_i. \quad (12)$$

By the spectral mapping theorem [35, Ch 2, Thm 2.4.], the eigenfunctions  $\psi_i$  are also eigenfunctions of the transfer operators  $\mathcal{T}_\tau$  for all  $\tau$ , corresponding to eigenvalues

<sup>1</sup> It is usually assumed that the potential satisfies some growth conditions, e.g.,  $V(x) \geq C_1 \|x\|^2$  for  $\|x\| \geq C_2$  for some  $C_1, C_2 > 0$ , to confine the process with overwhelming probability in bounded domains. We will assume this in the sequel too. This also means that we can restrict the process to sufficiently large bounded domains (either with reflecting or absorbing boundary conditions), while maintaining all its statistical properties up to vanishing errors, since the probability of paths leaving the domain tends to zero as the domain grows.

<sup>2</sup> On a bounded domain, the operator  $(\lambda - \mathcal{L})^{-1}$  is compact for a sufficiently large  $\lambda > 0$ , as can be seen from [35, Theorems 7.1.1, 7.2.2, and 7.2.3]. Thus, the eigenvalues of  $\mathcal{L}$  only accumulate at infinity, and are thus all isolated. Further,  $(\lambda - \mathcal{L})^{-1}$  and  $\mathcal{L}$  possess the same eigenfunctions.

$$\lambda_i(\tau) = e^{-\kappa_i \tau}. \quad (13)$$

Due to the exponential decay of all  $\lambda_i(\tau)$ , it is common to refer to the  $\kappa_i$  as rates, and to their reciprocals as implied timescales

$$t_i = \frac{1}{\kappa_i}. \quad (14)$$

The action of  $\mathcal{T}_\tau$  on a function  $f \in L_\mu^2$  can be decomposed as

$$\mathcal{T}_\tau f = \sum_{i=1}^{\infty} e^{-\kappa_i \tau} \langle f, \psi_i \rangle_\mu \psi_i. \quad (15)$$

In many applications, including molecular dynamics, we expect to find a *spectral gap*, that is a number  $M$  of dominant rates  $0 = \kappa_1 < \kappa_2 < \kappa_M \ll \kappa_{M+1}$  separated from all others. In this case, the expansion (15) consists of only  $M$  slowly decaying terms if  $t \gg t_{M+1}$ . The existence of dominant spectral components is directly related to metastability, that is, the existence of long-lived macrostates such that transitions between those states are rare events [10, 12, 13].

### 2.3 Markov State Models and Variational Approach

Many numerical methods for the analysis of metastable behavior have focussed on modeling the dominant eigenfunctions  $\psi_1, \dots, \psi_M$  by linear combinations of a finite set of basis functions  $\varphi_i$ ,  $i = 1, \dots, N$ . Applying either a Galerkin projection to the transfer operator  $\mathcal{T}_\tau$  [12, 42] or invoking the Rayleigh–Ritz variational principle [19, 30] leads to the generalized eigenvalue problem

$$C^\tau v_k = \hat{\lambda}_k C^0 v_k \quad (16)$$

$$C_{i,j}^\tau = \langle \mathcal{T}_\tau \varphi_i, \varphi_j \rangle_\mu, \quad (17)$$

$$C_{i,j}^0 = \langle \varphi_i, \varphi_j \rangle_\mu. \quad (18)$$

The top  $M$  generalized eigenvectors provide expansion coefficients for approximate eigenfunctions

$$\hat{\psi}_k = \sum_{i=1}^N v_{ki} \varphi_i, \quad k = 1, \dots, M. \quad (19)$$

Notably, the matrix elements in Eqs. (17–18) can be approximated by ergodic averages from long simulations. We refer to this approximation technique as the variational approach to conformational dynamics (VAC). If the basis functions are chosen as indicator functions corresponding to a decomposition of state space into non-overlapping sets  $S_i$ ,  $i = 1, \dots, N$ , Eq. (16) is also referred to as Ulam’s method or a Markov state model (MSM). In this case, the matrix  $T = (C^0)^{-1} C^\tau$ , which possesses the same eigenvalues as the solutions of Eq. (16), can be interpreted as a stochastic transition matrix between the sets  $S_i$ . This allows to make use of numerous tools available to analyze discrete time Markov chains. Please see Refs [42, 37, 43, 4] on the use of MSMs in biomolecular simulation, and the recent reviews [29, 20] on the VAC and its relation to other methods and fields. In the numerical examples (sec. 4), the VAC and MSMs are the primary tools we use to extract dominant spectral components from simulation data.

### 3 Projected Dynamics

If the state space dimension  $d$  is large, simulation of the dynamics Eq. (1) up to statistically relevant time horizons can be prohibitively costly. It is therefore desirable to perform a dimensionality reduction by projecting the system onto a much smaller number  $m$  of variables, and replace the full dynamics by a suitable effective dynamics that only depends on the selected degrees of freedom. Many different techniques to accomplish this have been developed. Here, we focus on the projection formalism introduced in Ref. [22] and discussed in detail in Ref. [46].

### 3.1 Projection Operator

Dimensionality reduction is realized by a function  $\xi$  which maps the state space  $\mathbb{R}^d$  onto  $\mathbb{R}^m$ , where  $m \leq d$ . We denote the components of the map  $\xi$  by  $\xi_l$ ,  $l = 1, \dots, m$ , and assume each component to be smooth, such that  $\xi_l \in D(\mathcal{L})$  for all  $l$ . Also, we assume that the image of  $\xi$  can be mapped to all of  $\mathbb{R}^m$  by a diffeomorphism. Without loss of generality, we can then take the image of  $\xi$  to be all of  $\mathbb{R}^m$ . The key ingredient to the definition of an effective dynamics that only depends on the lower-dimensional space  $\mathbb{R}^m$ , is the projection operator [46]

$$\mathcal{P}f(z) = \frac{1}{\nu(z)} \int_{\Sigma_z} f(x) \mu(x) J^{-1/2}(x) d\sigma_z(x). \quad (20)$$

In this definition,  $z \in \mathbb{R}^m$ ,  $\Sigma_z = \{x \in \mathbb{R}^d : \xi(x) = z\}$  is the pre-image of  $z$  under the map  $\xi$ , and  $\sigma_z$  denotes the surface measure on the set  $\Sigma_z$ . Moreover,  $J(x)$  is the Jacobian determinant of the map  $\xi$ , and

$$\nu(z) = \int_{\Sigma_z} \mu(x) J^{-1/2}(x) d\sigma_z(x) \quad (21)$$

is the  $\xi$ -marginal of  $\mu$  at  $\xi(x) = z$ . Thus, the projection operator acts on a function  $f \in L^2_\mu$  by averaging its values over the level sets of the map  $\xi$  with respect to the invariant measure. The additional factor  $J^{-1/2}$  and the appearance of the surface measure are due to the co-area formula [17] and account for the non-linear change of variables. The normalization by  $\nu(z)$  ensures that the projection of a constant function is the constant itself. We introduce the notation

$$d\mu_z(x) = \frac{1}{\nu(z)} \mu(x) J^{-1/2}(x) d\sigma_z(x) \quad (22)$$

for the probability measure on  $\Sigma_z$  obtained by conditioning the invariant measure  $\mu$  to  $\xi(x) = z$ . We also note that  $\nu$  is itself a probability density on  $\mathbb{R}^m$ ,

$$\int_{\mathbb{R}^m} \nu(z) dz = 1, \quad (23)$$

and hence gives rise to a probability measure which we will also denote by  $\nu$ .

For each  $f \in L^2_\mu$ , the function  $\mathcal{P}f$  depends on the variables  $z$  only. In fact,  $\mathcal{P}$  is an orthogonal projection onto the subspace

$$H_0 = \left\{ f \in L^2_\mu : \exists \tilde{f} : \mathbb{R}^m \rightarrow \mathbb{R}, f = \tilde{f} \circ \xi \right\} \quad (24)$$

spanned by functions of this type [2]. The subspace  $H_0$  can be identified with the space  $L^2_\nu$  of square-integrable functions on  $\mathbb{R}^m$  with respect to  $\nu$ , and the scalar products are identical for all  $f, g \in H_0$  [46]:

$$\langle f, g \rangle_\mu = \langle \tilde{f}, \tilde{g} \rangle_\nu. \quad (25)$$

For  $f \in H_0$  we identify  $f$  and  $\tilde{f}$  from now on, and we also write  $\nabla_z f(x)$  for  $\nabla_z \tilde{f}(\xi(x))$ . As usual, we denote the projection onto the orthogonal complement of  $H_0$  by  $\mathcal{P}^\perp = \mathcal{I} - \mathcal{P}$ .

### 3.2 Effective Dynamics

In Refs. [22, 46], it was suggested to define an effective dynamics  $Z_t$  on  $\mathbb{R}^m$ ,

$$dZ_t = b^\xi(Z_t)dt + \sqrt{2\beta^{-1}}\sigma^\xi(Z_t)dB_t, \quad (26)$$

by the following definitions of effective drift and diffusion:

$$b_l^\xi(z) = \mathcal{P}(\mathcal{L}\xi_l)(z), \quad l = 1, \dots, m \quad (27)$$

$$a_{lr}^\xi(z) = \left[ \begin{array}{c} (\sigma^\xi)^T \\ \sigma^\xi \end{array} \right]_{lr} (z) = \mathcal{P} \left( \nabla \xi_l^T a \nabla \xi_r \right) (z), \quad l, r = 1, \dots, m. \quad (28)$$

As discussed in detail in Ref. [46], these coefficients result from a Galerkin projection of the generator  $\mathcal{L}$  onto the infinite-dimensional space  $H_0 = L_\nu^2$ . Consider the operator

$$\mathcal{L}^\xi = \mathcal{P}\mathcal{L}\mathcal{P}, \quad (29)$$

which is a self-adjoint operator on  $D(\mathcal{L}^\xi) = D(\mathcal{L}) \cap H_0 \subset L_\nu^2$ . For twice differentiable functions  $f \in D(\mathcal{L}^\xi)$ , it also acts as a differential operator

$$\mathcal{L}^\xi f = \mathcal{P} [\mathcal{L}\xi] \cdot \nabla_z f \quad (30)$$

$$+ \frac{1}{\beta} \mathcal{P} \left[ \nabla \xi^T a \nabla \xi \right] : \nabla_z^2 f, \quad (31)$$

where  $\mathcal{L}\xi$  is understood componentwise and  $\nabla \xi$  is a  $d \times m$ -matrix,  $[\nabla \xi]_{il} = \frac{\partial \xi_l}{\partial x_i}$ . Thus,  $\mathcal{L}^\xi$  is the infinitesimal generator of a diffusion process on  $\mathbb{R}^m$  with drift and diffusion given by Eqs. (27-28). The effective drift and diffusion can also be calculated by the Kramers-Moyal formulae

$$b_l^\xi(z) = \lim_{s \rightarrow 0} \mathbb{E} \left[ \frac{1}{s} (\xi_l(X_s) - z_l) \middle| X_0 \sim \mu_z \right], \quad (32)$$

$$a_{lr}^\xi(z) = \frac{\beta}{2} \lim_{s \rightarrow 0} \mathbb{E} \left[ \frac{1}{s} (\xi_l(X_s) - z_l) (\xi_r(X_s) - z_r) \middle| X_0 \sim \mu_z \right]. \quad (33)$$

In practice, the expectations in Eqs. (32-33) must be estimated at a finite value of the parameter  $s$ , which we will call the *offset* from now on.

### 3.3 Preservation of Spectral Properties

We investigate conditions to ensure that the operator  $\mathcal{L}^\xi$  approximately preserves the dominant eigenvalues  $\kappa_1, \dots, \kappa_M$ , which encode the metastability of the process. We assume that  $\mathcal{L}^\xi$  also possesses a complete set of eigenfunctions  $\psi_i^\xi$  and corresponding eigenvalues  $-\omega_i$ . We follow the approach from previous works [46, 47, 2] and consider the case that the dominant eigenfunctions can be approximately parametrized by the projected variables, that is, we assume that

$$\psi_i(x) \approx \psi_i(z) = \psi_i(\xi(x)). \quad (34)$$

It was already shown in [46] that if Eq. (34) holds exactly, then the corresponding eigenvalues are left unchanged by the projection:

**Lemma 1** *Assume that  $\psi_i \in H_0$ , that is,  $\psi_i(x) = \psi_i(z)$ . Then  $\psi_i$  is also an eigenfunction of  $\mathcal{L}^\xi$  corresponding to the same eigenvalue  $-\kappa_i$ .*

In the next result, we show that if not only the eigenfunctions themselves, but also their derivatives can be well approximated by functions in  $H_0$ , a bound on the eigenvalue error for  $\mathcal{L}^\xi$  can be obtained:

**Proposition 1** *If, for each eigenfunction  $\psi_i$ ,  $i = 1, \dots, M$ , the error upon projection onto  $H_0$  is small in  $H_\mu^1$ -norm, i.e.,*

$$\|\mathcal{P}^\perp \psi_i\|_{H_\mu^1}^2 = \|\mathcal{P}^\perp \psi_i\|_{L_\mu^2}^2 + \sum_{j=1}^d \left\| \frac{\partial \mathcal{P}^\perp \psi_i}{\partial x_j} \right\|_{L_\mu^2}^2 \leq \epsilon^2, \quad (35)$$

then the maximal relative error between the dominant eigenvalues of  $\mathcal{L}^\xi$  and  $\mathcal{L}$  is bounded by

$$\max_{i=2, \dots, M} \frac{\omega_i - \kappa_i}{\omega_i} \leq (M-1) \kappa_2^{-1/2} \sqrt{\eta_1 \beta^{-1}} \epsilon. \quad (36)$$

*Proof* Note that by definition, the first eigenfunction  $\psi_1 \equiv 1$  is not affected by the projection, therefore we only consider the error for  $i = 2, \dots, M$ . Following the approach in Ref. [15], we choose some positive constant  $\alpha > 0$  and introduce the operator  $\mathcal{A} = \alpha \text{Id} - \mathcal{L}$ . Since  $\mathcal{L}$  is negative semi-definite by Eqs. (6) and (10),  $\mathcal{A}$  is positive definite, and therefore defines a norm on  $D(\mathcal{L})$

$$\|f\|_{\mathcal{A}}^2 = \langle \mathcal{A}f, f \rangle_\mu. \quad (37)$$

We consider the finite-dimensional space  $G$  spanned by the functions  $g_i := \mathcal{P}\psi_i$ , which we assume to be linearly independent without loss of generality. Let  $\mathcal{Q}_{\mathcal{A}}$  denote the  $\mathcal{A}$ -orthogonal projection onto  $G$ , and let  $\hat{\omega}_i$  denote the approximate eigenvalues generated by the Ritz-Galerkin projection onto  $G$ . Theorem 4.3 and Remark 4.2 in Ref. [15] provide us with the following estimate:

$$\max_{i=2, \dots, M} \frac{\hat{\omega}_i - \kappa_i}{\hat{\omega}_i} \leq (M-1) \max_{j=2, \dots, M} (\alpha + \kappa_j)^{-1/2} \|\mathcal{Q}_{\mathcal{A}}^\perp \psi_j\|_{\mathcal{A}}. \quad (38)$$

Examining the projection errors on the right-hand-side, we find

$$\|\mathcal{Q}_{\mathcal{A}}^\perp \psi_j\|_{\mathcal{A}}^2 \leq \|\psi_j - g_j\|_{\mathcal{A}}^2 \quad (39)$$

$$= \alpha \|\psi_j - g_j\|_{L_\mu^2}^2 - \langle \mathcal{L}(\psi_j - g_j), (\psi_j - g_j) \rangle_\mu \quad (40)$$

$$= \alpha \|\psi_j - g_j\|_{L_\mu^2}^2 + \frac{1}{\beta} \int_{\mathbb{R}^d} \langle a(x) \nabla(\psi_j - g_j)(x), \nabla(\psi_j - g_j)(x) \rangle d\mu(x), \quad (41)$$

by Eq. (10). As  $\psi_j - g_j = \psi_j - \mathcal{P}\psi_j = \mathcal{P}^\perp \psi_j$ , we conclude

$$\|\mathcal{Q}_{\mathcal{A}}^\perp \psi_j\|_{\mathcal{A}}^2 \leq \left(\alpha + \frac{\eta_1}{\beta}\right) \|\psi_j - g_j\|_{H_\mu^1}^2 \quad (42)$$

$$\leq \left(\alpha + \frac{\eta_1}{\beta}\right) \epsilon^2, \quad (43)$$

and since  $\alpha > 0$  was arbitrary, we end up with the result

$$\max_{i=2, \dots, M} \frac{\hat{\omega}_i - \kappa_i}{\hat{\omega}_i} \leq (M-1) \kappa_2^{-1/2} \sqrt{\eta_1 \beta^{-1}} \epsilon. \quad (44)$$

As discussed in Ref. [46, Sec. 3.2.3], Galerkin projection of the full generator onto a subspace of  $H_0$  is equivalent to a Galerkin projection of the projected generator  $\mathcal{L}^\xi$  onto the same subspace. From the Rayleigh-Ritz variational principle we obtain  $\hat{\omega}_i \geq \omega_i$ , thus we conclude

$$\frac{\omega_i - \kappa_i}{\omega_i} = 1 - \frac{\kappa_i}{\omega_i} \quad (45)$$

$$\leq 1 - \frac{\kappa_i}{\hat{\omega}_i} \quad (46)$$

$$= \frac{\hat{\omega}_i - \kappa_i}{\hat{\omega}_i}, \quad (47)$$

and the claim follows.

In Ref. [47, Theorem 2], it was shown that the *absolute* eigenvalue error of the projected generator is small if  $\|\mathcal{L}\mathcal{P}^\perp\psi_i\|_{L_\mu^2}$  and  $\|\mathcal{P}^\perp\psi_i\|_{L_\mu^2}$  are small. Proposition 1 complements these results in the sense that it bounds the *relative* error of eigenvalues (timescales), which is a more practical error measure for eigenvalues close to zero, i.e., large timescales. Furthermore, the bound (35) is less restrictive than the conditions in [47], as it uses a  $H_\mu^1$  norm instead of the  $H_\mu^2$  (or equivalent) norm, as done therein. In fact, the bound assumed in [47, Theorem 2] implies our bound (35) up to to a multiplicative constant.

**Proposition 2** *Let us consider the diffusion (1), satisfying (6), on a bounded domain with smooth boundary and reflecting boundary conditions. If  $\|\mathcal{L}\mathcal{P}^\perp\psi_i\|_{L_\mu^2} \leq \delta_1$ , then there is a  $C > 0$  such that the assumptions of Prop. 1 are satisfied with*

$$\|\mathcal{P}^\perp\psi_i\|_{H_\mu^1} \leq C\delta_1. \quad (48)$$

*Proof* Since the spatial domain is bounded and  $\mu$  is smooth, it is a weight in Muckenhoupt class, cf. [6, Eq. (1.2)]. The regularity conditions [6, Eqs. (2.2)–(2.4)] are satisfied by assumption. Now, the result follows directly from the weighted Agmon–Douglis–Nirenberg estimate [6, Theorem 2.4] giving  $\|u\|_{H_\mu^2} \leq C\|\mathcal{L}u\|_{L_\mu^2}$  for some  $C > 0$  independent of  $u$ . We have

$$\|\mathcal{P}^\perp\psi_i\|_{H_\mu^1} \leq \|\mathcal{P}^\perp\psi_i\|_{H_\mu^2} \quad (49)$$

$$\leq C\|\mathcal{L}\mathcal{P}^\perp\psi_i\|_{L_\mu^2} \quad (50)$$

$$\leq C\delta_1, \quad (51)$$

concluding the proof.

### 3.4 Langevin Dynamics

So far, we have discussed spectral properties of the projected dynamics for reversible diffusion processes. A widespread dynamical model, especially in molecular simulations, are the Langevin dynamics, Eqs. (3-4). These dynamics are, however, not reversible in full state space. Nevertheless, in many molecular dynamics applications, the slow transitions of interest are typically independent of the momentum coordinates, which can be assumed to equilibrate rapidly. It is also well-known that under a re-scaling of time and for large friction  $\gamma$ , the spatial dynamics are close to a reversible overdamped process. More precisely, upon re-scaling time via  $(q_t^\epsilon, p_t^\epsilon) = (q_{t/\epsilon}, p_{t/\epsilon})$ , and choosing  $\epsilon = \frac{1}{\gamma}$ , Eqs. (3-4) transform to

$$dq_t^\epsilon = \frac{1}{\epsilon}p_t^\epsilon dt, \quad (52)$$

$$dp_t^\epsilon = -\frac{1}{\epsilon}\nabla V(q_t^\epsilon)dt - \frac{1}{\epsilon^2}p_t^\epsilon dt + \frac{1}{\epsilon}\sqrt{2\beta^{-1}}dB_t. \quad (53)$$

As it is well-known (see, e.g., [33], [25]), the theory of multiscale asymptotics shows that, as  $\epsilon \rightarrow 0$ , the re-scaled positional dynamics Eq. (52) converge weakly to the overdamped Langevin process

$$dq_{\tilde{t}} = -\nabla V(q_{\tilde{t}})d\tilde{t} + \sqrt{2\beta^{-1}}dB_{\tilde{t}}. \quad (54)$$

Thus, conditional expectations like Eq. (8) or Eqs. (32-33) converge to those estimated from overdamped Langevin dynamics Eq. (54) as  $\epsilon \rightarrow 0$ . Moreover, we note that Eq. (54) is obtained from Eq. (5) by the same re-scaling of time,  $\tilde{t} = t/\epsilon = \gamma t$ .

As re-scaling of time is the same as observing a process at larger time window, we can exploit this finding by selecting a sufficiently large offset  $s$  in the Kramers–Moyal formulae Eqs. (32-33) for a reaction coordinate  $\xi$  which is independent of the momenta. If both the friction  $\gamma$  and the offset  $s$  are sufficiently large, the effective drift and diffusion obtained by the Kramers–Moyal formulae can be expected to approximately agree with those of the overdamped process Eq. (5) estimated at the same offset. This enables us to estimate an effective dynamics from Langevin dynamics data for which the approximation results from section 3.3 still apply.

Using a large offset  $s$  in the Kramers–Moyal formulae seems to be at odds with the need to use a small value of  $s$  in order to remain close to the actual limit  $s \rightarrow 0$ . However, we have found compelling numerical evidence

that even at surprisingly large values of  $s$ , good approximations to the dominant eigenvalues of the transfer operator  $\mathcal{T}_\tau$  can be obtained from the effective simulations (i.e., from the transfer operator  $\mathcal{T}_\tau^\xi$  of the effective process). We will discuss these findings in the numerical examples below. A rigorous result on this phenomenon is still missing. In the next section, we take a first step and characterize the expected drift and diffusion for large values of  $s$  if  $z$  is contained in an idealized metastable set.

### 3.5 Asymptotics for Large Offsets

We use the notation  $b_l^{\xi,s}$ ,  $a_{lr}^{\xi,s}$  for the components of effective drift and diffusion estimated at finite  $s$ . Assuming a timescale separation as described in section 2.2, there exist  $M$  subsets  $S_i \subset \mathbb{R}^d$  such that the  $M$  first eigenfunctions of the generator are nearly constant within the sets  $S_i$ :  $\psi_j(x) \approx \rho_{ij}$  if  $x \in S_i$  [11]. Let us assume that there are corresponding subsets  $\tilde{S}_i \subset \mathbb{R}^m$  such that  $\Sigma_z \subset S_i$  for all  $z \in \tilde{S}_i$ , i.e., the level sets of all points in  $\tilde{S}_i$  are completely contained within the metastable set  $S_i$ . This is in line with the idea that our choice of reaction coordinates should be able to parametrize the dominant eigenfunctions well. Using these assumptions, we can show the following:

**Proposition 3** *Given the assumptions outlined above, for  $z \in \tilde{S}_i$  and for  $s \gg t_{M+1}$ , the effective drift and diffusion satisfy*

$$b_l^{\xi,s}(z) \approx \frac{1}{s}(c_l^i - z_l), \quad (55)$$

$$c_l^i = \sum_{j=1}^M e^{-\kappa_j s} \langle \xi_l, \psi_j \rangle_\mu \rho_{ij}, \quad (56)$$

$$a_{lr}^{\xi,s}(z) \approx \frac{\beta}{2s} \left( z_l z_r - c_r^i z_l - c_l^i z_r + c_{lr}^i \right) \quad (57)$$

$$c_{lr}^i = \sum_{j=1}^M e^{-\kappa_j s} \langle \xi_l \xi_r, \psi_j \rangle_\mu \rho_{ij}. \quad (58)$$

*Proof* We express the effective drift at finite  $s$  using Ito's formula:

$$b_l^{\xi,s}(z) = \frac{1}{s} \mathbb{E} [(\xi_l(X_s) - z_l) | X_0 \sim \mu_z] \quad (59)$$

$$= \frac{1}{s} \mathbb{E} \left[ \int_0^s \mathcal{L} \xi_l(X_t) dt + \int_0^s \nabla \xi_l(X_t) \cdot dB_t | X_0 \sim \mu_z \right] \quad (60)$$

$$= \frac{1}{s} \mathbb{E} \left[ \int_0^s \mathcal{L} \xi_l(X_t) dt | X_0 \sim \mu_z \right] \quad (61)$$

$$= \frac{1}{s} \int_0^s \int_{\Sigma_z} \mathbb{E}^x [\mathcal{L} \xi_l(X_t)] d\mu_z(x) dt, \quad (62)$$

where we have used the fact that the stochastic integral is of zero expectation. Next, we apply the identities

$$\mathbb{E}^x [f(X_\tau)] = \mathcal{T}_\tau f(x), \quad (63)$$

$$\frac{d}{d\tau} \mathcal{T}_\tau f = \mathcal{T}_\tau \mathcal{L} f, \quad (64)$$

for  $f \in D(\mathcal{L})$ , to obtain:

$$b_l^{\xi,s}(z) = \frac{1}{s} \int_{\Sigma_z} \int_0^s \mathcal{T}_t \mathcal{L} \xi_l(x) dt d\mu_z(x) \quad (65)$$

$$= \frac{1}{s} \int_{\Sigma_z} \int_0^s \frac{d}{dt} \mathcal{T}_t \xi_l(x) dt d\mu_z(x) \quad (66)$$

$$= \frac{1}{s} \int_{\Sigma_z} (\mathcal{T}_s - \text{Id}) \xi_l(x) d\mu_z(x). \quad (67)$$

$$= \frac{1}{s} \left[ \int_{\Sigma_z} \mathcal{T}_s \xi_l(x) d\mu_z(x) - z_l \right]. \quad (68)$$

Inserting the spectral expansion Eq. (15) and truncating it after  $M$  terms, we find:

$$b_l^{\xi,s}(z) = \frac{1}{s} \left[ \int_{\Sigma_z} \sum_{j=1}^M e^{-\kappa_j s} \langle \xi_l, \psi_j \rangle_{\mu} \psi_j(x) d\mu_z(x) - z_l \right] \quad (69)$$

$$\approx \frac{1}{s} \left[ \sum_{j=1}^M e^{-\kappa_j s} \langle \xi_l, \psi_j \rangle_{\mu} \rho_{ij} - z_l \right] \quad (70)$$

$$= \frac{1}{s} (c_l^i - z_l). \quad (71)$$

In the second equation, we used the assumption about constancy of the eigenfunctions along the levelset  $\Sigma_z$ . The result for the diffusion can be obtained in a similar way, by re-writing the Kramers-Moyal formula Eq. (33) as

$$a_{lr}^{\xi,s}(z) = \frac{\beta}{2s} \mathbb{E} [(\xi_l(X_s) - z_l)(\xi_r(X_s) - z_r) | X_0 \sim \mu_z] \quad (72)$$

$$= \frac{\beta}{2s} \mathbb{E} [(\xi_l(X_s)\xi_r(X_s) - z_l z_r) - z_l(\xi_r(X_s) - z_r) - z_r(\xi_l(X_s) - z_l) | X_0 \sim \mu_z]. \quad (73)$$

Now, we follow the previous derivation separately for each of the three terms in the expectation, and use that the pre-factors  $z_l$  and  $z_r$  for the last two terms are not affected by the expectation. This results in

$$a_{lr}^{\xi,s}(z) \approx \frac{\beta}{2s} \left[ (c_{lr}^i - z_l z_r) - z_l (c_r^i - z_r) - z_r (c_l^i - z_l) \right] \quad (74)$$

$$= \frac{\beta}{2s} \left[ z_l z_r - z_l c_r^i - z_r c_l^i + c_{lr}^i \right]. \quad (75)$$

## 4 Numerical Examples

In all of the following examples, we use the Kramers-Moyal formulae Eqs. (32-33) to obtain numerical estimates of effective drift and diffusion from simulation data of the original process Eq. (1). These expressions suggest to use the following procedure: for each point  $z \in \mathbb{R}^m$ , we need to draw a large number of initial conditions from the distribution  $\mu_z$  along the level set  $\Sigma_z$ . Independent simulations need to be started from each of these points and run for a short time  $s$ . Averages of the linear and quadratic differences  $\frac{1}{s}(\xi(X_s) - z)$  and  $\frac{1}{s}(\xi(X_s) - z) \otimes (\xi(X_s) - z)$  over all simulations provide estimates of the effective drift and diffusion at point  $z$ . However, as all of the examples below are rather simple systems, we can proceed differently in this work. We start out with a long equilibrium simulation of the full process  $X_t$ . We discretize the reaction coordinate space into discrete bins  $B_i$ . For each of these bins, all simulation steps  $X_t$  such that  $\xi(X_t)$  falls into  $B_i$  are determined. As the data is in global equilibrium, we can then average the linear and quadratic differences  $\frac{1}{s}(\xi(X_{t+s}) - \xi(X_t))$  and  $\frac{1}{s}(\xi(X_{t+s}) - \xi(X_t)) \otimes (\xi(X_{t+s}) - \xi(X_t))$  over all  $X_t \in B_i$  to obtain discretized estimates of effective drift and diffusion. These estimates are extended to continuous space by interpolation. This procedure is feasible as long as the reaction coordinate space is low-dimensional and simulation of an equilibrium trajectory is possible, as it is in all of the following examples. If the reaction coordinate space is not low-dimensional, we recommend to obtain functional representations of effective drift and diffusion by means of the data-based regression explained in Ref. [3]. Moreover, if equilibrium data cannot be produced, re-weighting methods such as those explained in Refs. [44, 45, 21] need to be employed on top of that.

### 4.1 Lemon Slice Potential

Our first numerical example is a two-dimensional toy system. We consider overdamped Langevin dynamics Eq. (5) in the ‘‘lemon slice’’ potential [2]

$$V(r, \varphi) = \cos(7\varphi) + 10(r-1)^2 + \frac{1}{r} + 0.05, \quad (76)$$

where  $r, \varphi$  are two-dimensional polar coordinates, at inverse temperature  $\beta = 1$  and friction  $\gamma = 1$ . The structure of the potential function suggests that its slow dynamics correspond to transitions between the seven minima shown in Fig. 1. It follows that the polar angle  $\varphi$  should parametrize the first seven eigenfunctions of the associated generator well, making it an appropriate choice of reaction coordinate:

$$\xi(x, y) = \varphi(x, y). \quad (77)$$

In this case, the effective drift  $b^\xi$  and diffusion  $a^\xi$  can be calculated analytically, see appendix A:

$$b^\xi(z) = \frac{7C_1}{C_2} \sin(7z) \quad (78)$$

$$a^\xi(z) = \frac{C_1}{C_2} \quad (79)$$

$$C_1 = \int_0^\infty \frac{1}{r} \exp(-10(r-1)^2 - \frac{1}{r}) dr \quad (80)$$

$$C_2 = \int_0^\infty r \exp(-10(r-1)^2 - \frac{1}{r}) dr. \quad (81)$$

We generate a long equilibrium simulation of the dynamics Eq. (5) using the Euler–Maruyama method at integration time step  $\Delta_t = 10^{-3}$  for a total of  $10^7$  steps. A Markov state model analysis—as described in section 2.3—of the full data set reveals seven dominant eigenvalues and six corresponding slow timescales  $t_2, \dots, t_7$ , as expected. As indicated in Fig. 2 C, these slow timescales come in three pairs due to the symmetry of the system. Their numerical values are  $t_2 \approx t_3 \approx 1.70$ ,  $t_4 \approx t_5 \approx 0.49$ ,  $t_6 \approx t_7 \approx 0.29$ .

By the procedure outlined at the beginning of this section, we estimate the parameters of the effective dynamics using 63 discrete bins along the angular coordinate, each of bin width 0.1 radians. We do so for a range of different offsets  $s$  between the integration time step  $s = 10^{-3}$  up to  $s = 1$ . We can observe in Figs. 2 A and B that, as expected, the exact drift and diffusion Eqs. (78-79) are recovered well for small  $s$ , while very different results are obtained as  $s$  increases. Nevertheless, we run simulations of the effective dynamics using all of these estimates of drift and diffusion, at the same integration time step and total simulation length as in the original dynamics. All of these simulations are analyzed by a Markov state model, where the same bins as above are used as discrete states. As shown in Fig. 2 C, the resulting estimates of the six leading implied timescales barely change as  $s$  increases. Only the last two timescales  $t_6, t_7$  start deviating from the reference as  $s$  approaches the magnitude of  $t_6, t_7$  themselves, which is not surprising. Similarly, we monitor the stationary probabilities of the seven potential minima if estimated from the different effective simulations. The minima are defined as intervals  $z \in [z_k - 0.25, z_k + 0.25]$  for  $z_k = -\pi + \frac{2\pi k}{7}$ ,  $k = 0, \dots, 6$ . We compare them to the reference obtained by numerically integrating the marginal  $\nu(z)$ , Eq. (21), over those intervals. In Fig. 2 D, we find that these probabilities are preserved by the effective dynamics until  $s$  is comparable to  $t_6, t_7$ . Thus, the essential stationary and dynamical properties of the original dynamics seem to be preserved even if the effective dynamics are estimated at fairly large offset  $s$ , which is a surprising result.

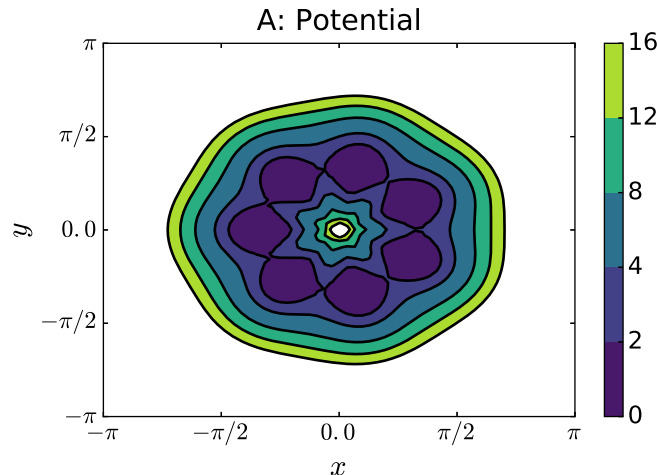


**Figure 1** Contour plot of the lemon slice potential Eq. (76).

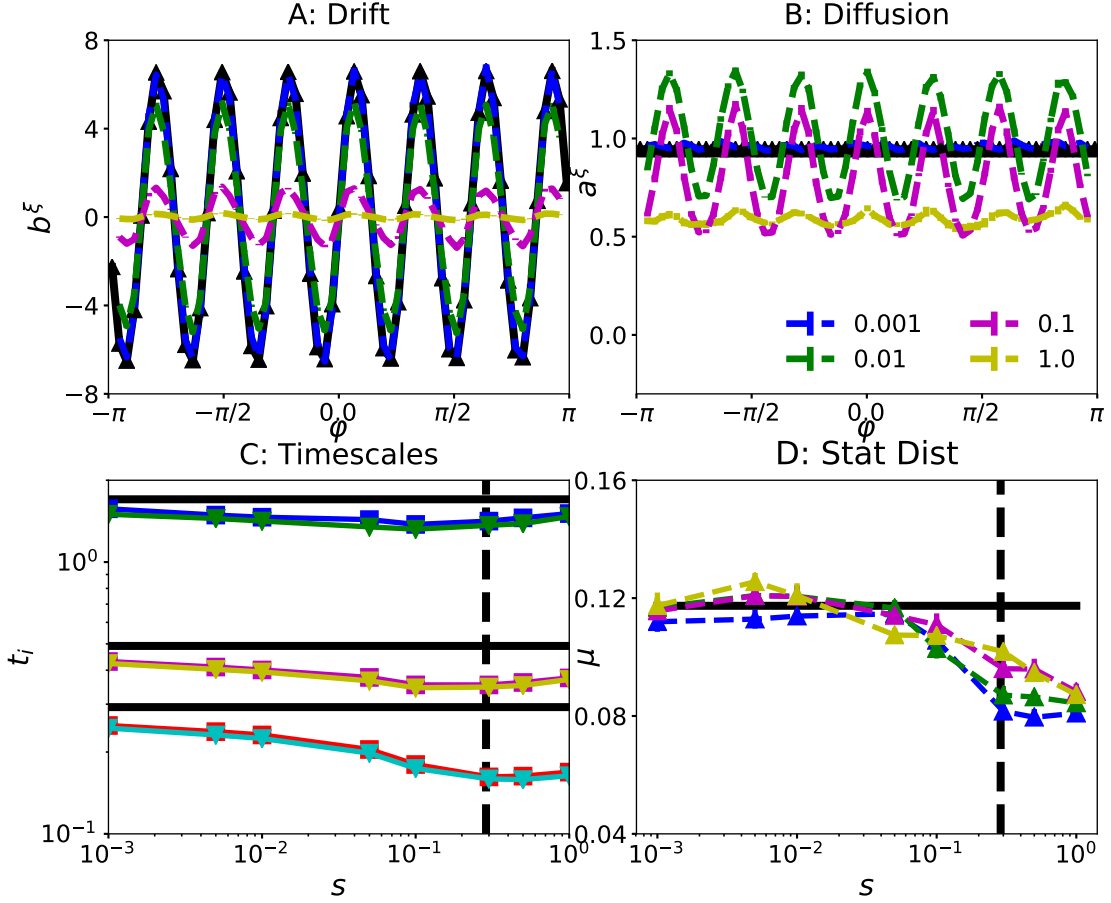


**Figure 2** Analysis of effective dynamics on the polar angle for the lemon slice potential. A: Numerical estimates of effective drift for different values of the offset  $s$ , compared to the reference in black. B: The same for the effective diffusion. C: Implied timescales  $t_2, \dots, t_7$  obtained by analyzing simulation data of the effective dynamics, as a function of  $s$ , compared to the reference values in black. Note that all of these timescales come in three pairs due to the symmetry of the system. The vertical dashed line indicates the last two dominant timescales  $t_6 \approx t_7$ . D: Stationary probabilities of the potential minima estimated from simulations of the effective dynamics, as a function of  $s$  (we only show four of the seven stationary probabilities for clarity of the figure). The reference value is shown in black, it is the same for all seven minima. The vertical dashed line indicates the last two dominant timescales  $t_6 \approx t_7$ . Errorbars were produced by bootstrapping on the original data (A and B) and on the effective simulations (C and D). We note that errorbars in C and D are barely visible.

#### 4.2 Langevin Toy Model

Next, we study Langevin dynamics in another two-dimensional toy potential. The potential is composed of a double-well in  $x$ -direction and a harmonic potential in both  $x$  and  $y$ , the functional form is

$$V(x, y) = 1.5(x - 2)^4 - 9(x - 2)^2 + 3x + 0.5(x - 2)^2 + 0.5(y - 2)^2. \quad (82)$$

A contour plot of  $V$  is shown in Fig. 3. We set  $\gamma = 10$ ,  $\beta = 0.4$ . The slowest transition in this energy landscape is the crossing of the barrier around  $x = 2$ , the corresponding implied timescale is  $t_2 \approx 75$ . We project the system onto the  $x$ -coordinate only, integrating out all momentum coordinates. We note that the effective dynamics provided by Eqs. (27-28), in the limit of  $s \rightarrow 0$ , are meaningless in this case. It can be verified that  $b^\xi(x) = a^\xi(x) = 0$  for all  $x$ . In brief terms, the reason is that the dynamics are anti-symmetric in the momentum coordinate  $p$ , while  $\mu$  is symmetric in  $p$ , and thus the projection  $\mathcal{P}$  integrates over an odd function in  $p$ ; see [41, 1]. However, upon increasing the offset it is possible to find a sweet spot where  $s$  is larger than the momentum relaxation time  $\frac{1}{\gamma}$ , but smaller than the slowest timescale  $t_2$ . In this regime, the overdamped limit can be exploited to find a meaningful effective dynamics along  $x$ . We also note that the effective dynamics would not vanish if the first momentum coordinate was included in the projection.

We simulate Langevin dynamics using the Euler–Maruyama scheme at integration time step  $\Delta_t = 10^{-2}$  for  $10^7$  steps, and also generate data of the overdamped dynamics in the same potential using the same simulation parameters. Figures 4 A and B show numerical estimates of the effective drift and diffusion obtained by the Kramers–Moyal formulae along 24 discrete bins of bin width 0.2, using both the Langevin and overdamped Langevin simulations. We note that these estimates are very different for  $s = 0.01$  (and indeed, estimates from Langevin data are close to zero), but agree for  $s = 1.0$ . Again, we produce long simulations of all the resulting effective dynamics, and analyze these data by a Markov state model defined on the same discrete bins as above, extracting the slowest implied timescale  $t_2$  and the probabilities of the two metastable sets using the PCCA method [14, 38]. We find that for sufficiently large  $s$ , all effective simulations reproduce both  $t_2$  (Fig. 4 C) and the probabilities of the PCCA sets (Fig. 4 D) from the original simulations of the overdamped dynamics.

This example shows that the overdamped limit can be exploited by using a sufficiently large offset  $s$ , and again, we find that essential stationary and dynamical properties of the original dynamics are retained by effective simulations estimated at large  $s$ .

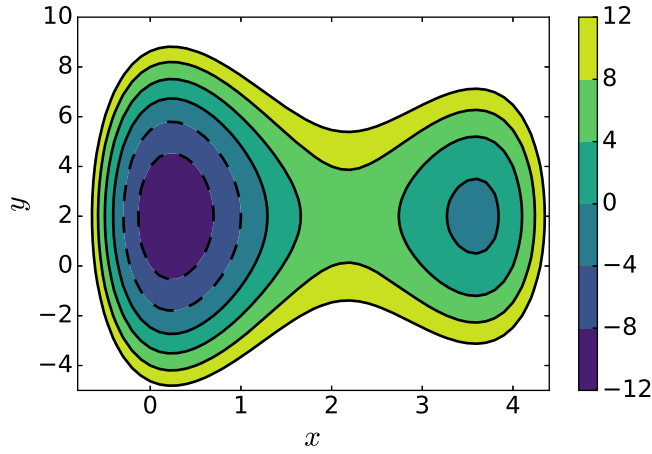


**Figure 3** Contour plot of the two-dimensional toy potential Eq. (82).

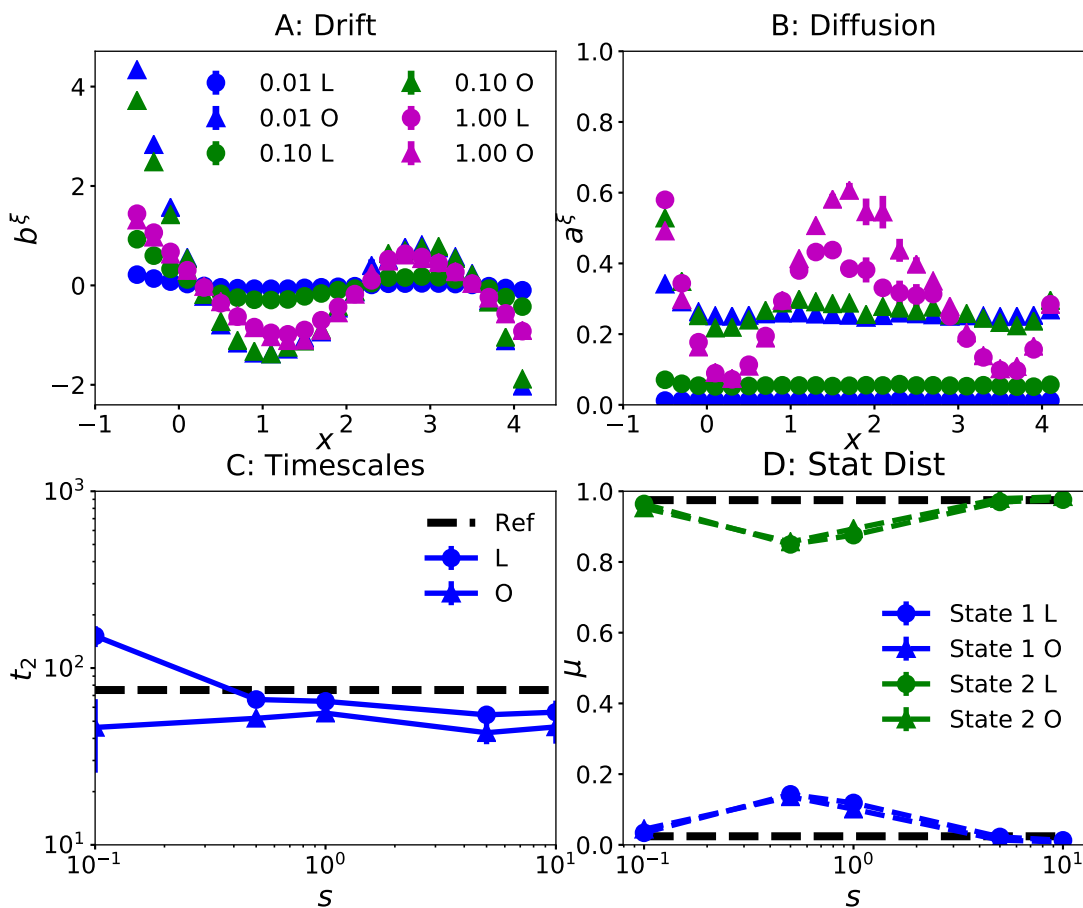


**Figure 4** Analysis of effective dynamics on the  $x$ -coordinate of the two-dimensional toy potential Eq. (82). A: Numerical estimates of effective drift for different values of the offset  $s$  (indicated by different colors) using both the Langevin (L) data (circles) and the overdamped (O) data (triangles). B: The same for the effective diffusion. C: Leading implied timescale  $t_2$  obtained by analyzing simulation data of the effective dynamics from both Langevin data (circles) and overdamped data (triangles), as a function of  $s$ , compared to the reference value in black. D: Stationary probabilities of the two metastable sets estimated from simulations of the effective dynamics from both Langevin data (circles) and overdamped data (triangles), as a function of  $s$ , compared to the references in black. Errorbars were produced by bootstrapping on the original data (A and B) and on the effective simulations (C and D). We note that errorbars in C and D are barely visible.

### 4.3 Alanine Dipeptide

Our next example is a dataset of molecular dynamics simulations of alanine dipeptide. This small molecule consists of only a single amino acid with two capping groups. It has been used as a test system for numerous methods and algorithms in the past years. Its slow dynamics can be described by the backbone dihedral angles  $\phi$ ,  $\psi$ . The projected free energy in  $\phi$ - $\psi$ -space decomposes into three minima, and the highest barrier to be crossed is aligned with the  $\phi$ -direction, as shown in Fig. 5 A. The corresponding implied timescale is  $t_2 \approx 1.5$  ns [32]. Therefore, we choose  $\xi(x) = \phi(x)$  as one-dimensional reaction coordinate in this example, lumping the two states on the left into a single metastable state. To avoid numerical difficulties caused by unsampled regions of reaction coordinate space, we make use of the periodicity of the dihedral angles and shift the interval  $[\frac{3}{4}\pi, \pi]$  to  $[-\frac{5}{4}\pi, -\pi]$  in what follows. The range of  $\xi$  thus becomes  $\xi(x) \in [-\frac{5}{4}\pi, \frac{3}{4}\pi]$ .

The system was simulated in explicit water using the Amber99 force field and velocity re-scaling thermostat, see Ref. [32] for a detailed simulation setup. The data consists of 20 long simulations of 200 ns simulation time each, resulting in  $4 \mu\text{s}$  total simulation time. Each simulation is long enough to sample the global equilibrium distribution. The velocity re-scaling thermostat has been shown to be closely related to Langevin dynamics [5]. It also involves a smallness parameter (called  $\tau$  in [5]), which is related to the friction via  $\tau = (2\gamma)^{-1}$ . Its numerical value is  $\tau = 0.01$  ps in this data set. We expect to find similar results as in the case of Langevin dynamics. A Markov state model based on 500 discrete bins in  $\phi$ - $\psi$ -space serves as reference model.

The effective drift and diffusion are estimated for 62 discrete bins along the  $\phi$ -coordinate. The bin width is 0.1, and offsets ranging from  $s = 1$  ps up to  $s = 500$  ps are used. Instead of showing all of these parameters here, we provide an illustration of the local approximations Eqs. (55-57) within the two metastable sets along  $\phi$  at a large offset ( $s = 100$  ps). We find in Fig. 5 B that they are in good agreement with the Kramers–Moyal estimates. Just as in the previous examples, we use all of the estimated parameters and produce simulations of the effective dynamics in  $\phi$  by means of the Euler scheme. The same integration time step is employed as in the original MD simulations, and each of those trajectories covers 200 ns of total simulation time. Figure 5 C shows the slowest implied timescale estimated by Markov state models of the effective simulations, based on the same discrete bins used above, as a function of  $s$ . It can be observed that the slowest timescale is massively underestimated at small  $s$ , but estimates improve with increasing  $s$  and the correct regime is reached for  $s \geq 100$  ps. Furthermore, we use PCCA to extract two dominant metastable states from the effective simulations. We calculate their stationary probabilities and compare them to those of the dominant metastable states in the original simulation. The results in Fig. 5 D confirm that at sufficiently large offset, these stationary probabilities agree.

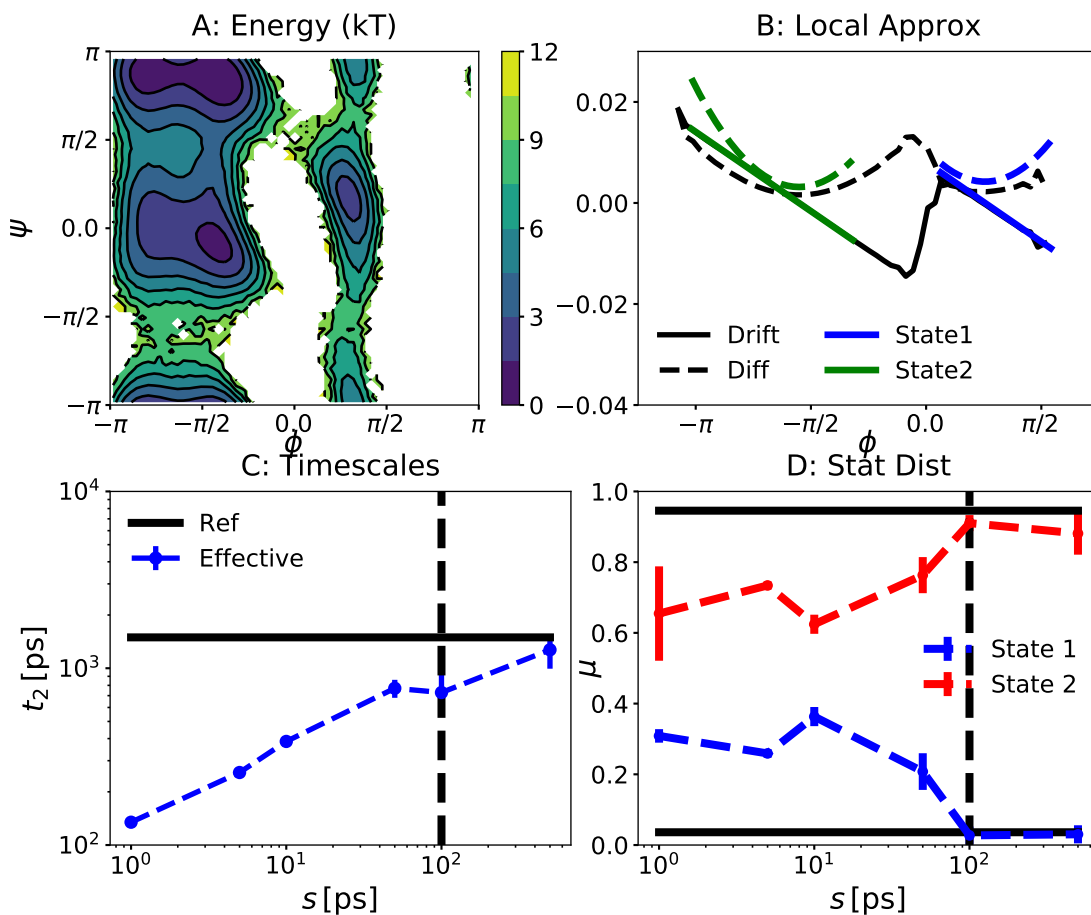


**Figure 5** Analysis of effective dynamics for alanine dipeptide along  $\phi$ -direction. A: Effective free energy of the original simulation data in  $\phi$ - $\psi$ -space. B: Comparison of numerical estimates for drift and diffusion at  $s = 100$  ps to the local approximations Eqs. (55-57) within the two dominant metastable sets of the original dynamics. We use blue and green color to indicate the local approximations within the two states, while the numerical estimates are shown in black. The drift is represented by a solid line and the diffusion by a dashed line. C: Slowest implied timescale  $t_2$  obtained from a Markov state model of the effective dynamics, as a function of  $s$ . The reference value is indicated by the black line. The vertical dashed line indicates where the offset equals  $\frac{1}{\tau}$ , which is where the overdamped regime is expected to be attained. D: Stationary probabilities of two PCCA sets extracted from the effective dynamics, as a function of  $s$ . Black lines indicate stationary probabilities of metastable sets extracted from the original data. The vertical dashed line indicates where the offset equals  $\frac{1}{\tau}$ , which is where the overdamped regime is expected to be attained. Errorbars in panels C and D were obtained by bootstrapping on the effective simulations.

#### 4.4 Deca Alanine

We conclude by studying a set of more complex molecular simulation data. The deca alanine peptide has also been used as a test system in multiple previous studies. Here, we use a data set of six independent long simulations of 500 ns each, using the Amber03 force field and velocity re-scaling thermostat with time constant  $\tau = 0.01$  ps, see Ref. [32] for the complete simulation setup. It was also shown in Ref. [32] that the slowest dynamical process is formation and deformation of a helix, it occurs at an implied timescale  $t_2 \approx 7.6$  ns, followed by the next slowest process at  $t_3 \approx 3.9$  ns.

This time, we select a two-dimensional projection into the space of two slowest approximate eigenfunctions, that is  $\xi(x) = [\hat{\psi}_2(x), \hat{\psi}_3(x)] \in \mathbb{R}^2$ , where  $\hat{\psi}_2 \approx \psi_2$ ,  $\hat{\psi}_3 \approx \psi_3$ . These approximations are obtained by the following procedure: we apply TICA [36] to the the time series of 16 backbone dihedral angles in the peptide. According to the criterion of kinetic variance [28,27], the first seven TICs are retained, and the  $k$ -means algorithm is used to discretize this space into 500 states. The  $k$ -means clustercenters are used as centers for a basis of 500 isotropic multivariate Gaussian functions with covariance matrix equal to 0.5 times the identity. As described in section 2.3, the optimal linear approximations  $\hat{\psi}_2, \hat{\psi}_3$  to the first two eigenfunctions of  $\mathcal{T}_\tau$  projected on this basis are computed by the VAC, completing the definition of  $\xi$ . The upper part of Fig. 6 A shows the free energy  $-\frac{1}{\beta} \log(\nu(z))$  in this space, where three major minima can be identified. Based on 100  $k$ -means clusters in the seven-dimensional TICA space mentioned above, we build a Markov state model which serves as reference.

We use 784 bins of size  $0.1 \times 0.1$  in the projected space to estimate effective drift and diffusion for a series of offsets between  $s = 1$  ps and  $s = 1$  ns, and employ the Euler scheme to run the resulting stochastic dynamics at integration time step 2 fs for 500 ns total simulation time. We extract the two leading implied timescales from all of these simulations using a Markov state model on the same discrete states as above, and compare them to those of the original simulation in Fig. 6 B. Both timescales are massively underestimated at small  $s$ , but agree well as  $s$  approaches 1 ns. In Fig. 6 A, lower part, we show the effective free energy sampled by the simulation at  $s = 1$  ns. It can be seen that detailed features of the original energy landscape are washed out, only the overall structure of valleys and barriers is roughly preserved. Nevertheless, comparing the stationary probabilities of the three PCCA sets obtained from the original dynamics in both the original and effective simulations, we find that these probabilities are approximately preserved for  $s = 1$  ns. In fact, they are preserved for most values of  $s$  in this example, see Fig. 6 C. Again, we find that, while detailed features of the original simulations are lost if a large offset  $s$  is used, the essential (long-timescale) dynamical and stationary properties remain unchanged.

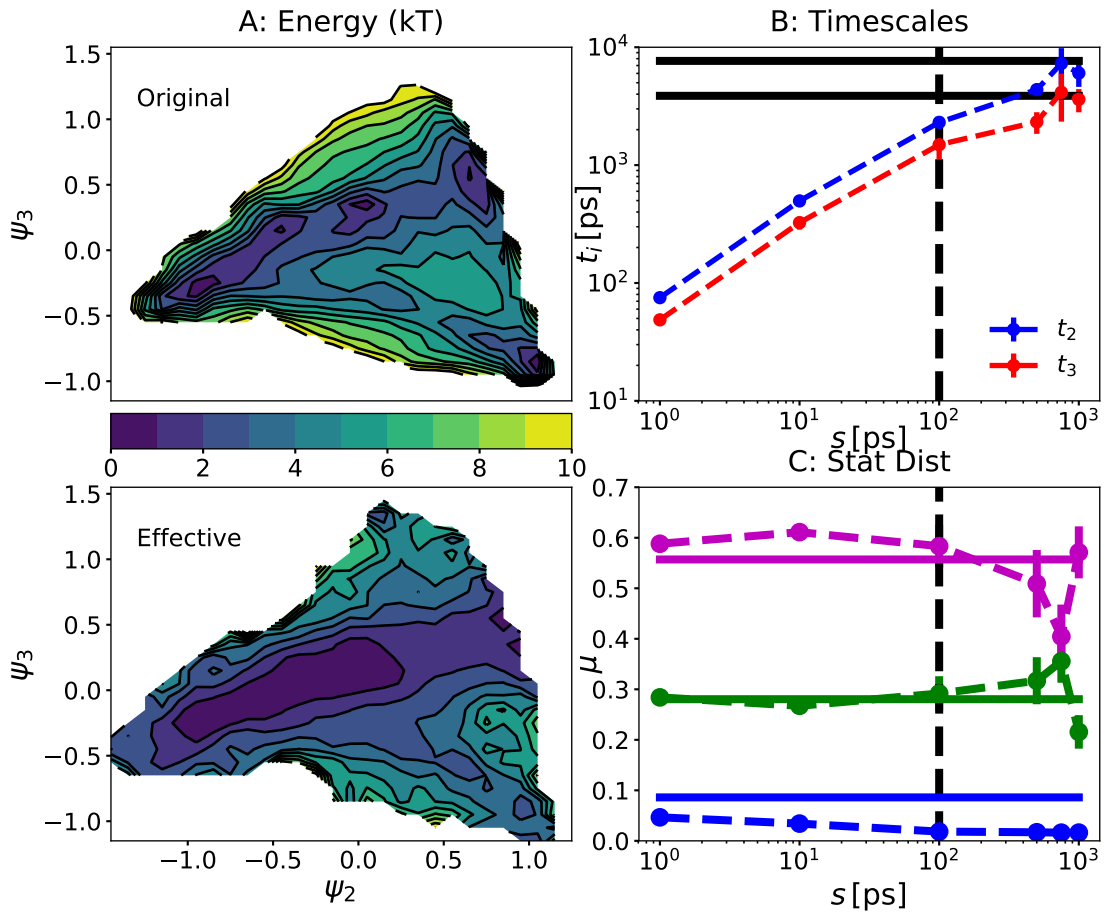


**Figure 6** Analysis of effective dynamics for deca alanine in the space of its two slowest eigenfunctions. A: Effective free energy of the original dynamics (top) and free energy sampled by effective dynamics at  $s = 1$  ns (bottom). B: First two implied timescales of the effective simulations as a function of the offset  $s$ , compared to the references in black. The vertical dashed line indicates where the offset equals  $\frac{1}{\tau}$ , which is where the overdamped regime is expected to be attained. C: Stationary probabilities of three metastable sets (obtained from the original data using the PCCA method) as a function of  $s$  (dashed lines), compared to the reference values (solid lines). The vertical dashed line indicates where the offset equals  $\frac{1}{\tau}$ , which is where the overdamped regime is expected to be attained. Errorbars in panels B and C were obtained by bootstrapping on the effective simulations.

## 5 Summary

We have discussed the approximation of high-dimensional diffusion processes by effective dynamics defined on the lower-dimensional space of reduced variables. We have analyzed the approximation quality of low-lying eigenvalues of the corresponding generator for reversible diffusions. A new relative error bound for dominant eigenvalues in terms of the  $H_\mu^1$ -approximation error of the corresponding eigenfunctions was proved. Furthermore, we have discussed how the overdamped limit can be exploited to extend the validity of these approximation results to Langevin dynamics. Numerical examples have shown that using a large offset in the Kramers-Moyal estimators for effective drift and diffusion coefficients does not seem to impair the approximation quality of dominant eigenvalues. Future work will focus on providing a theoretical foundation for the observations stated in this paper.

## Acknowledgments

We would like to thank Ralf Banisch, Stefan Klus, Thomas Swinburne, Tony Lelièvre and Frank Noé for fruitful discussions. This work was supported by the National Science Foundation (Nos. CHE-1265929, CHE-1738990, and PHY-1427654) and the Welch Foundation (No. C-1570). F.N. is a postdoctoral researcher in the

Rice University Academy of Fellows. P.K. is supported by Deutsche Forschungsgemeinschaft (DFG) through CRC 1114 "Scaling Cascades in Complex Systems", project A01, and the Einstein Foundation Berlin (Einstein Center ECMath). We are also indebted to the Institute for Pure and Applied Mathematics (IPAM) for hosting the long program "Complex High-Dimensional Energy Landscapes". The program was immensely beneficial to this work.

## Appendix

### A Lemon Slice Potential

Here, we calculate the effective drift and diffusion if the lemon slice potential Eq. (76) is projected onto the polar angle  $\xi(x, y) = \varphi(x, y)$ . We start by expressing the generator  $\mathcal{L}$  in polar coordinates. The Laplacian operator in polar coordinates is

$$\Delta f = \frac{\partial^2 f}{\partial r^2} + \frac{1}{r^2} \frac{\partial^2 f}{\partial \varphi^2} + \frac{1}{r} \frac{\partial f}{\partial r}. \quad (83)$$

Moreover, it follows from the chain rule and the definition of  $\xi$  that for any function  $f$ ,

$$\frac{\partial f}{\partial x} = \cos \varphi \frac{\partial f}{\partial r} - \frac{\sin \varphi}{r} \frac{\partial f}{\partial \varphi}, \quad (84)$$

$$\frac{\partial f}{\partial y} = \sin \varphi \frac{\partial f}{\partial r} + \frac{\cos \varphi}{r} \frac{\partial f}{\partial \varphi}. \quad (85)$$

The generator in polar coordinates then becomes

$$\mathcal{L} = - \left[ \frac{\partial V}{\partial r} \frac{\partial}{\partial r} + \frac{1}{r^2} \frac{\partial V}{\partial \varphi} \frac{\partial}{\partial \varphi} \right] + \frac{1}{\beta} \left[ \frac{\partial^2}{\partial r^2} + \frac{1}{r^2} \frac{\partial^2}{\partial \varphi^2} + \frac{1}{r} \frac{\partial}{\partial r} \right]. \quad (86)$$

Applying the generator to the reaction coordinate  $\xi$ , only one of the terms above is non-zero, resulting in

$$\mathcal{L}\xi = - \frac{1}{r^2} \frac{\partial V}{\partial \varphi} = \frac{7}{r^2} \sin(7\varphi). \quad (87)$$

In order to evaluate Eq. (27), we note that the Jacobian determinant of  $\xi$  is  $J(x, y) = \frac{1}{r^2}$ , and that the stationary distribution factors, canceling the  $\varphi$ -dependent and the constant term. The normalization  $\nu(z) = \nu(\varphi)$  thus equals  $C_2$ , and the effective drift becomes

$$b^\xi(\varphi) = \frac{1}{\nu(\varphi)} \int_0^\infty \frac{7}{r^2} \sin(7\varphi) r \mu(r, \varphi) dr \quad (88)$$

$$= \frac{7}{C_2} \sin(7\varphi) \int_0^\infty \frac{1}{r} \exp(-10(r-1)^2 - \frac{1}{r}) dr \quad (89)$$

$$= \frac{7C_1}{C_2} \sin(7\varphi). \quad (90)$$

For the diffusion, we obtain

$$\nabla \xi^T a \nabla \xi = \left( \frac{\partial \xi}{\partial x} \right)^2 + \left( \frac{\partial \xi}{\partial y} \right)^2 \quad (91)$$

$$= J(x, y) = \frac{1}{r^2}. \quad (92)$$

Inserting this into Eq. (28) and using the same arguments as before, we end up with Eq. (79).

## References

1. Bittracher, A., Koltai, P., Junge, O.: Pseudogenerators of spatial transfer operators. *SIAM J. Appl. Dyn. Syst.* **14**(3), 1478–1517 (2015)
2. Bittracher, A., Koltai, P., Klus, S., Banisch, R., Dellnitz, M., Schütte, C.: Transition Manifolds of Complex Metastable Systems: Theory and Data-Driven Computation of Effective Dynamics. *J. Nonlinear Sci. (Md)*, 1–42 (2017)

3. Boninsegna, L., Nüske, F., Clementi, C.: Sparse learning of stochastic dynamical equations. *J. Chem. Phys.* **148**(24), 241,723 (2018)
4. Bowman, G.R., Pande, V.S., Noé, F. (eds.): *An Introduction to Markov State Models and Their Application to Long Timescale Molecular Simulation*. Springer Netherlands (2014)
5. Bussi, G., Parrinello, M.: Stochastic thermostats: comparison of local and global schemes. *Comput. Phys. Commun.* **179**(1-3), 26–29 (2008)
6. Cejas, M.E., Durán, R.G.: Weighted a priori estimates for elliptic equations. *Studia Mathematica* (2018)
7. Chorin, A.J., Hald, O.H., Kupferman, R.: Optimal prediction and the Mori–Zwanzig representation of irreversible processes. *Proc. Natl. Acad. Sci. U.S.A.* **97**(7), 2968–2973 (2000)
8. Chorin, A.J., Hald, O.H., Kupferman, R.: Optimal prediction with memory. *Physica D* **166**(3), 239–257 (2002)
9. Clementi, C.: Coarse-grained models of protein folding: Tol-models or predictive tools? *Curr. Opin. Struct. Biol.* **18**, 10–15 (2008)
10. Davies, E.B.: Metastable states of symmetric Markov semigroups I. *Proc. London Math. Soc.* **45**, 133–150 (1982)
11. Davies, E.B.: Metastable states of symmetric Markov semigroups II. *J. London Math. Soc.* **s2-26**(3), 541–556 (1982)
12. Dellnitz, M., Junge, O.: On the Approximation of Complicated Dynamical Behavior. *SIAM J. Numer. Anal.* **36**(2), 491–515 (1999)
13. Deuffhard, P., Huisinga, W., Fischer, A., Schütte, C.: Identification of almost invariant aggregates in reversible nearly uncoupled Markov chains. *Linear Algebra Appl.* **315**(1-3), 39–59 (2000)
14. Deuffhard, P., Weber, M.: Robust Perron cluster analysis in conformation dynamics. *Linear Algebra Appl.* **398**, 161–184 (2005)
15. Djurdjevac, N., Sarich, M., Schütte, C.: Estimating the Eigenvalue Error of Markov State Models. *Multiscale Model. Simul.* **10**(1), 61–81 (2012)
16. Evans, L.C.: *Partial differential equations*. American Mathematical Society (2010)
17. Evans, L.C., Gariepy, R.F.: *Measure theory and fine properties of functions*. CRC press (2015)
18. Hijón, C., Español, P., Vanden-Eijnden, E., Delgado-Buscalioni, R.: Mori–Zwanzig formalism as a practical computational tool. *Faraday Discuss.* **144**(0), 301–322 (2009)
19. Huisinga, W.: Metastability and dominant eigenvalues of transfer operators. *New algorithms Macromol. Simul.* pp. 1–17 (2006)
20. Klus, S., Nüske, F., Koltai, P., Wu, H., Kevrekidis, I., Schütte, C., Noé, F.: Data-Driven Model Reduction and Transfer Operator Approximation. *J. Nonlinear Sci.* (2018)
21. Koltai, P., Wu, H., Noé, F., Schütte, C.: Optimal data-driven estimation of generalized Markov state models for non-equilibrium dynamics. *Computation* **6**(1), 22 (2018)
22. Legoll, F., Lelièvre, T.: Effective dynamics using conditional expectations. *Nonlinearity* **23**(9), 2131 (2010)
23. Legoll, F., Lelièvre, T., Olla, S.: Pathwise estimates for an effective dynamics. *Stochastic Processes Appl.* **127**(9), 2841–2863 (2017)
24. Lelièvre, T., Stoltz, G.: *Partial differential equations and stochastic methods in molecular dynamics*. *Acta Numer.* **25**, 681–880 (2016)
25. Lelièvre, T., Stoltz, G., Rousset, M.: *Free Energy Computations: A Mathematical Perspective*. Imperial College Press (2010)
26. Mori, H.: Transport, collective motion, and Brownian motion. *Prog. Theor. Phys.* **33**, 423–455 (1965)
27. Noé, F., Banisch, R., Clementi, C.: Commute Maps: Separating Slowly Mixing Molecular Configurations for Kinetic Modeling. *J. Chem. Theory Comput.* **12**(11), 5620–5630 (2016)
28. Noé, F., Clementi, C.: Kinetic Distance and Kinetic Maps from Molecular Dynamics Simulation. *J. Chem. Theory Comput.* **11**(10), 5002–5011 (2015)
29. Noé, F., Clementi, C.: Collective variables for the study of long-time kinetics from molecular trajectories: theory and methods. *Curr. Opin. Struct. Biol.* **43**, 141–147 (2017)
30. Noé, F., Nüske, F.: A variational approach to modeling slow processes in stochastic dynamical systems. *Multiscale Model. Simul.* **11**, 635–655 (2013)
31. Noid, W.G.: Perspective: Coarse-grained models for biomolecular systems. *J. Phys. Chem.* **139**(9), 090,901 (2013)
32. Nüske, F., Keller, B.G., Pérez-Hernández, G., Mey, A.S.J.S., Noé, F.: Variational Approach to Molecular Kinetics. *J. Chem. Theory Comput.* **10**, 1739–1752 (2014)
33. Pavliotis, G., Stuart, A.: *Multiscale methods: averaging and homogenization*. Springer Science & Business Media (2008)
34. Pavliotis, G.A.: *Stochastic Processes and Applications*. Springer New York (2014)
35. Pazy, A.: *Semigroups of linear operators and applications to partial differential equations*. Springer, New York, Berlin (1983)
36. Pérez-Hernández, G., Paul, F., Giorgino, T., De Fabritiis, G., Noé, F.: Identification of slow molecular order parameters for Markov model construction. *J. Chem. Phys.* **139**(1), 15,102 (2013)
37. Prinz, J.H., Wu, H., Sarich, M., Keller, B., Senne, M., Held, M., Chodera, J.D., Schütte, C., Noé, F.: Markov models of molecular kinetics: Generation and Validation. *J. Chem. Phys.* **134**, 174,105 (2011)
38. Röblitz, S., Weber, M.: Fuzzy spectral clustering by PCCA+: Application to Markov state models and data classification. *Adv. Data Anal. Classif.* **7**(2), 147–179 (2013)
39. Rohrdanz, M.A., Zheng, W., Maggioni, M., Clementi, C.: Determination of reaction coordinates via locally scaled diffusion map. *J. Chem. Phys.* **134**, 124,116 (2011)
40. Saunders, M.G., Voth, G.A.: Coarse-graining methods for computational biology. *Annu. Rev. Biophys.* **42**(1), 73–93 (2013)
41. Schütte, C.: *Conformational dynamics: Modelling, theory, algorithm, and application to biomolecules* (1999)
42. Schütte, C., Fischer, A., Huisinga, W., Deuffhard, P.: A Direct Approach to Conformational Dynamics Based on Hybrid Monte Carlo. *J. Comput. Phys.* **151**(1), 146–168 (1999)
43. Schütte, C., Sarich, M.: *Metastability and Markov State Models in Molecular Dynamics: Modeling, Analysis, Algorithmic Approaches*. Courant Lecture Notes. American Mathematical Society and Courant Institute of Mathematical Sciences (2013)
44. Wu, H., Noé, F.: Spectral Learning of Dynamic Systems from Nonequilibrium Data. In: D.D. Lee, M. Sugiyama, U.V. Luxburg, I. Guyon, R. Garnett (eds.) *Adv. Neural Inf. Process. Syst.* 29, pp. 4179–4187. Curran Associates, Inc. (2016)

- 
45. Wu, H., Nüske, F., Paul, F., Klus, S., Koltai, P., Noé, F.: Variational approximation of molecular kinetics from short off-equilibrium simulations. *J. Chem. Phys.* (2017)
  46. Zhang, W., Hartmann, C., Schutte, C.: Effective dynamics along given reaction coordinates, and reaction rate theory. *Faraday Discuss.* **195**, 365–394 (2016)
  47. Zhang, W., Schütte, C.: Reliable Approximation of Long Relaxation Timescales in Molecular Dynamics. *Entropy* **19**(7) (2017)
  48. Zwanzig, R.: Nonlinear generalized Langevin equations. *J. Stat. Phys.* **9**(3), 215–220 (1973)